

Spintronic Hodgkin-Huxley-Analogue Neuron Implemented with a Single Magnetic Tunnel Junction

Davi R. Rodrigues,^{1,*} Rayan Moukhader^{2,3}, Yanxiang Luo⁴, Bin Fang,⁴ Adrien Pontlevy,² Abbas Hamadeh⁵, Zhongming Zeng⁴, Mario Carpentieri,^{1,†} and Giovanni Finocchio^{2,‡}


¹*Department of Electrical and Information Engineering, Politecnico di Bari, Bari 70125, Italy*

²*Department of Mathematical and Computer Sciences, Physical Sciences and Earth Sciences, University of Messina, Messina I-98166, Italy*

³*Multi-Disciplinary Physics Laboratory, Faculty of Sciences, Lebanese University, Beirut 1500, Lebanon*

⁴*Key Laboratory of Multifunctional Nanomaterials and Smart Systems, Suzhou Institute of Nano-Tech and Nano-Bionics, CAS, Suzhou, Jiangsu 215123, People's Republic of China*

⁵*Fachbereich Physik and Landesforschungszentrum OPTIMAS, Technische Universität Kaiserslautern, Kaiserslautern 67663, Germany*

 (Received 22 February 2023; revised 13 April 2023; accepted 26 April 2023; published 2 June 2023)

Spiking neural networks aim to emulate the brain's properties to achieve similar parallelism and high processing power. A caveat of these neural networks is the high computational cost for emulation, while current proposals for analogue implementations are energy inefficient and not scalable. We propose a device based on a single magnetic tunnel junction to perform neuron firing for spiking neural networks without the need for any resetting procedure. We leverage two areas of physics, magnetism and thermal effects, to obtain biorealistic spiking behavior analogous to the Hodgkin-Huxley model of the neuron. The device is also able to emulate the simpler leaky-integrate-and-fire model. Numerical simulations using experimental-based parameters demonstrate firing frequency in the megahertz to gigahertz range under constant input at room temperature. The compactness, scalability, low cost, CMOS compatibility, and power efficiency of magnetic tunnel junctions advocates for their broad use in hardware implementations of spiking neural networks.

DOI: [10.1103/PhysRevApplied.19.064010](https://doi.org/10.1103/PhysRevApplied.19.064010)

I. INTRODUCTION

Spiking neural networks (SNNs) are the third generation of artificial neural networks and promise a significantly reduction in energy consumption, especially for sparse time-dependent data [1–8]. The implementation of biologically plausible algorithms, which are associated with low power consumption and the ability to perform non-machine-learning computations, uphold their applications as robust artificial intelligence accelerators and computing devices while saving battery life. In SNNs, just as in biological brains, information is encoded in the relative time between asynchronous spiking events, which creates collective behavior in a topologically complex network of neurons. The sparse number of events, characterized by high information content, is responsible for the significantly reduced energy consumption and efficient response to event-based excitations. So far, SNNs have achieved remarkable success in the domains of visual processing

[9,10], speech recognition [11], and medical diagnosis [12].

Scalable SNNs that have some degree of stochasticity competitively emulate brain functions due to their highly parallel operation and *in situ* memory and processing. [4–6] Software simulations of biorealistic neuron synapses and firing are not competitive because they suffer from a high memory and processing cost, even though they are able to precisely emulate the current neuron models [9,13–18]. Hardware implementations of SNNs are proposed to overcome this obstacle [19]. They significantly increase the efficiency of the network by exploiting optimized task-specific components that mimic brain functionalities [4,8,20,21]. However, current implementation proposals are unable to optimally fulfill the requirements of SNNs [4,7,16,22]. Current neuromorphic systems, such as IBM's TrueNorth [23] and Intel's Loihi [24], exploit conventional complementary metal oxide semiconductor (CMOS) technology and rely mostly on architecture improvements to increase the neural network's efficiency [25]. Implementation of different materials and devices, nonetheless, will allow for better integration of the necessary neuromorphic properties directly at the material or device level by

*davi.rodrigues@poliba.it

†mario.carpentieri@poliba.it

‡gfinocchio@unime.it

leveraging their nonlinear functional response [1,26–29]. In particular, compact task-oriented devices can substitute complex CMOS circuits to increase scalability and energy efficiency. Memristors, for example, have attracted much attention due to their potential ability to mimic the spiking behavior and synaptic plasticity [30–34]. A promising alternative is the use of spintronic devices, which are characterized by low energy dissipation, non-volatility, high speed, reduced sizes, etc. [1,35–40]. The demonstrated integration with CMOS-based architectures and the advances in modeling tools of spintronic-CMOS hybrid systems [41] allows for the proposal of optimized spintronic components that can significantly increase area, energy, and memory efficiency of current hardware implementations of neural networks [28,29,42,43]. In particular, magnetic tunnel junctions (MTJs) are already shown to mimic synapse plasticity and firing [1,37–39,44–49].

Recently, MTJ-based devices have been proposed to emulate the leaky-integrate-and-fire (LIF) model of neurons, which has low computational costs [38,44,45]. These MTJ-based proposals rely solely on the magnetization dynamics generated by a series of pulses, which, when integrated over time, produce a single switch of the magnetization. A common caveat of these proposals is the requirement for a reset current pulse in the opposite direction to return the MTJ to the initial condition. The need for a reset mechanism also implies a clocking system, which significantly reduces the computational speed. To overcome the need for a resetting system, the use of MTJs in the stochastic regime, where the magnetization switches between the maximum and minimal resistance configuration due to thermal fluctuations [50,51], has been proposed. This paradigm suffers from the fact that true spikes are not obtained, since the switch of magnetization is not immediately followed by reverse switching. Moreover, the highly stochastic nature of these devices leads to a high error rate, which significantly increases the computational time. Other proposals that do not require a resetting mechanism involve the use of antiferromagnetic materials [35,36]. These proposals, however, suffer from the need for a single-domain ground state and, in the case of true sharp spikes, the presence of an applied alternate current [35]. A recent spiking MTJ-based proposal showed that combining the stochastic behavior and ferro-antiferromagnetic coupling allowed for the emulation of spiking with single pulses without the need for a resetting pulse [52]. Despite these advances towards the hardware implementation of the computationally cheap LIF model, a scalable room-temperature device that emulates more biorealistic neuron models is still lacking.

Biorealistic neuron models, such as the Hodgkin-Huxley (H-H) model [30,33,53–56], exhibit firing at a constant rate for a constant input, called tonic spiking, and allow for spike time-dependent plasticity (STDP) [57–59] and other biorealistic learning techniques [56,60]. The H-H model

TABLE I. A comparison between the H-H model and single MTJ device. The performance of the single MTJ device is based on experimental results [62].

	H-H model	Single MTJ device
Output	In terms of membrane potential	In terms of electrical resistance of the device
Physical mechanisms	Interplay between the concentrations of Na ⁺ and K ⁺ with leakage currents	Interplay between magnetization dynamics and thermal effects
Neuron behavior	Tonic spiking of the voltage at constant input current	Tonic spiking of the voltage at constant input current
Firing rates	1–10 kHz [55,63–66]	100 MHz–5 GHz
Applied voltage	1–200 mV [55,66,67]	100–300 mV
Refractory period	Present	Present

embodies the higher efficiency of the brain, and the firing behavior derives from the combination of the different response times of physical processes in the neuron. Here, we propose a single MTJ device that emulates biorealistic neurons that fire at frequencies in the megahertz to gigahertz range by leveraging thermal effects and Joule heating. The device produces sharp firing signals followed by a refractory period, which is essential for the implementation of biorealistic learning processes, such as STDP. For a comparison between the H-H model and the behavior of the single MTJ device proposed here, see Table I. We show that, with a single constant input, the device at room temperature fires at constant rate and presents a small, but not vanishing, stochasticity due to the thermal field [61]. A single firing response can also be obtained by integrating discrete pulses, and thus, the device also emulates the LIF model. The proposed device employs a single MTJ, which renders it CMOS-compatible, compact, robust, scalable, and reproducible, as required for SNNs. The device design proposed here is based on the idea of hybrid MTJs having the anisotropic easy axis of the free layer perpendicular to the in-plane polarizer. The main advantage of this solution is the ultralow-current working regime and self-oscillation at zero external field, as already demonstrated experimentally [62].

The proposed device concept is presented in detail as follows. In Sec. II, we describe the device properties and model. In Sec. III, we show the results obtained from micromagnetic simulations. In Sec. IV, we compare the behavior of the device and the H-H model. In Sec. V, we demonstrate the efficiency of the device in a SNN considering rate-based information encoding. Finally, Sec. VI provides a summary and outlook.

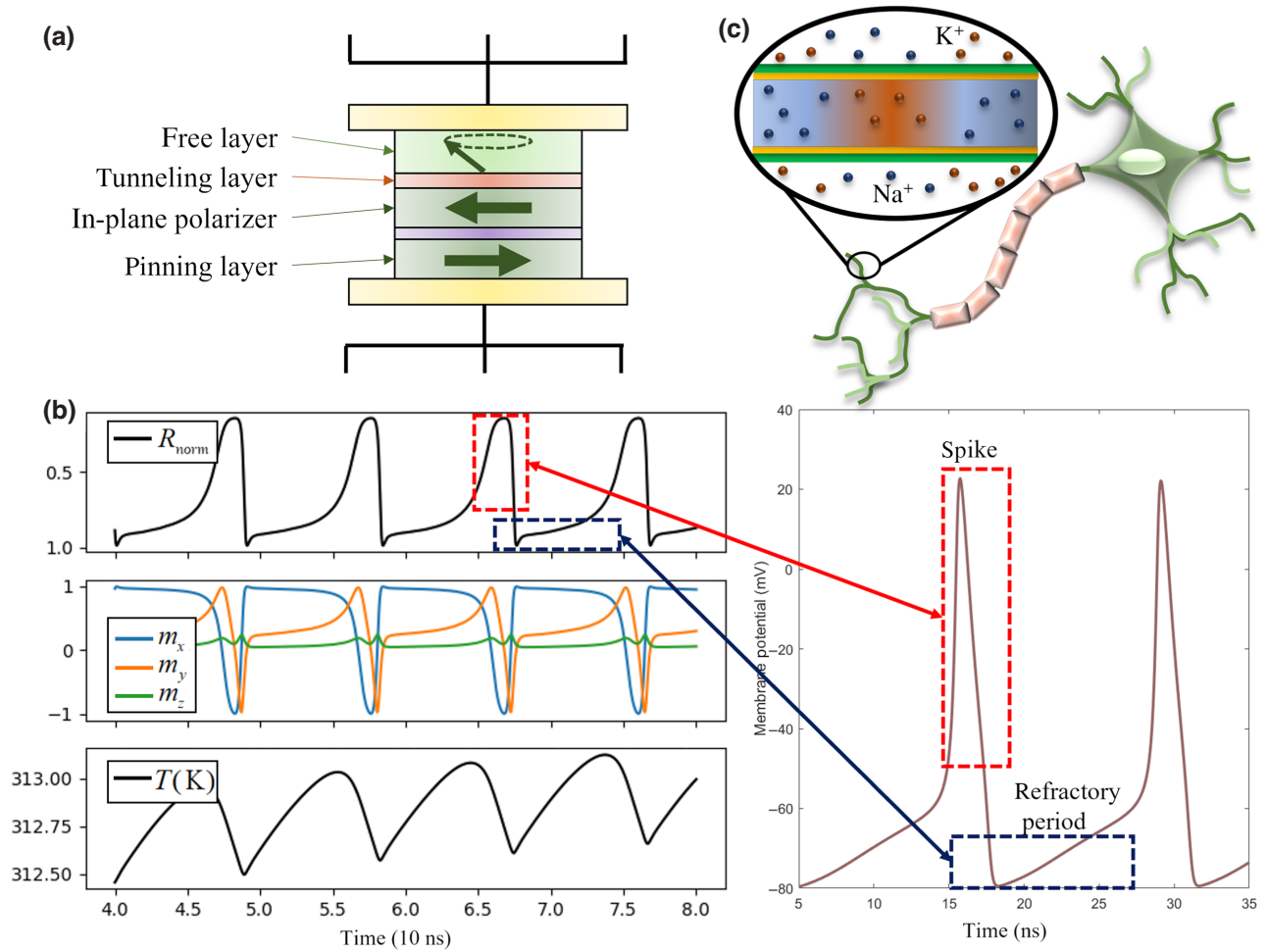


FIG. 1. MTJ implementation of biorealistic firing behavior. (a) Left, a sketch of the device concept of the proposed MTJ spiking device; right, a sketch of a biological neuron. Both receive the input in terms of currents and produce an output in terms of a voltage variation. In the spintronic device, the potential variation is due to changes in resistance produced by the input current and thermal effects. In the neuron, the potential variation is due to sodium (Na^+), potassium (K^+), and leakage currents. (b),(c) Comparison of resistance variation of the proposed MTJ device with the potential spiking in a biological neuron, according to the Hodgkin-Huxley model. In (b), from top to bottom, spikes in the resistance through the device, dynamics of the magnetization components, and temperature variation of the device. (c) Example of a numerical simulation of the dynamics of a H-H neuron. It can be observed that the behavior of a sharp firing signal followed by a refractory period is a common feature in both models. For a comparison between the two neurons, see Table I.

II. DEVICE AND MODEL

The overall design of the proposed device is shown in Fig. 1(a). Like a biological neuron, the device generates voltage spikes due to an applied current corresponding to the weighted sum of all signals received from other neurons. However, while the variation of the membrane potential in the biological neuron is due to sodium (Na^+), potassium (K^+), and leakage currents, the variation of the potential through the MTJ corresponds to a change in the resistance and is induced by the input current and thermal effects. The active part of the MTJ proposed here has a hybrid configuration, where the free-layer equilibrium configuration of magnetization is out of plane, and the

polarizer is in plane. As discussed extensively in the experimental work [62], this MTJ configuration has distinct behavior compared to MTJs, where the easy axis of the free layer is along the direction of magnetization in the fixed layer. In this case, the auto-oscillation generated by the spin-transfer torque (STT) induces an oscillation of the resistance, since the free-layer magnetization rotates between a state of maximum and minimum resistance, i.e., antiparallel and parallel to the polarizer, respectively. The resistance variation in a MTJ generates the spiking behavior described in Fig. 1(b), which is characterized by a sharp change in resistance followed by a refractory period, where the resistance reaches the highest values. Experiments demonstrate that this MTJ concept exhibits

an ultralow current-density threshold ($<10^6$ A/cm²) for excitation of the auto-oscillation [62].

The ultralow threshold is achieved by considering a polarizer composed of a synthetic antiferromagnet that allows for proper control of dipolar fields, which drive a small tilting of the equilibrium magnetization of the free layer at zero external field. The relative resistance of the MTJ is given by

$$R_{\text{norm}} = \frac{1 + P^2}{1 - P^2(\mathbf{m} \cdot \mathbf{p})}, \quad (1)$$

where $\mathbf{m} = \mathbf{M}/M_s$ is the unitary magnetization vector of the free layer, M_s is the magnetization saturation, $P < 1$ is the polarization, and \mathbf{p} is the direction of the spin-polarized current. Hence, in the absence of STT [68–71], the resistance of the MTJ is not at a minimum (\mathbf{m} and \mathbf{p} in the same direction) or maximum (\mathbf{m} and \mathbf{p} in opposite directions) state, since the magnetization of the free layer is perpendicular to the magnetization of the polarizer ($\mathbf{m} \cdot \mathbf{p} \approx 0$). When a polarized spin current along the maximum resistance direction is applied, the STT drives a large-amplitude magnetization precession.

To couple the magnetization dynamics with thermal effects, we consider three phenomena:

(1) *Resistance-variation-driven gain loss.* The first is associated with the gain loss of temperature of the MTJ driven by variations of the resistance:

$$\frac{dT}{dt} = \rho \frac{R_{\text{norm}}(JA)^2}{k_B} - \frac{(T - T_{\text{amb}})}{\tau_0}, \quad (2)$$

where T is the temperature of the MTJ, ρ is the heating efficiency, J is the applied current density, A is the area of the MTJ, k_B is the Boltzmann constant, T_{amb} is room temperature, and τ_0 is the natural temperature-decay time of the MTJ. The coefficient $\rho = R_0 t_b / 2\lambda$ depends on the maximum resistance of device R_0 , thickness t_b , and thermal conductivity λ of the free layer.

(2) *Parameter scaling.* The second phenomenon is given by the temperature scaling of the micromagnetic parameters, such as the magnetization saturation of the free layer [72] and the polarization [72–75],

$$M_s(T) = M_{s,0}(1 - (T/T_C)^{1.5}), \quad (3a)$$

$$P(T) = P_0(M_s(T)/M_{s,0})^{\varepsilon_P}, \quad (3b)$$

where T_C is the Curie temperature; $M_{s,0}$ and P_0 are the magnetization saturation and polarization, respectively, at $T = 0$ K; and ε_P is a scaling coefficient.

(3) *Stochasticity.* The third phenomenon is the thermal excitation of magnetization in the free layer, which produces a stochasticity of the magnetization trajectory.

Thermal excitation is incorporated as temperature-induced white noise, with magnitude [61,76]

$$h_{\text{ther}} = \sqrt{\frac{2k_B\alpha T}{M_s\gamma V_{\text{FL}}\Delta t}}, \quad (4)$$

where α is the phenomenological Gilbert damping, γ is the gyromagnetic ratio, V_{FL} is the volume of the free layer, and Δt is the simulation time step.

The first phenomenon describes the time evolution of the temperature, which, due to the second phenomenon, defines the time evolution of the material parameters. This combined physics is essential to ensure the transient stability of the magnetization in the higher-resistivity state and is thus crucial for the characteristic sharp spiking behavior. The third phenomenon generates the stochasticity inherent to biorealistic neural computation and is beneficial for neural network algorithms [1,3,4,77]. The role of each behavior is detailed in the next section.

To describe the magnetization dynamics, we consider a macrospin model based on the Landau-Lifshitz-Gilbert (LLG) equation in the presence of spin-orbit torques [69,78,79]:

$$\begin{aligned} \frac{d\mathbf{m}}{dt} = & -\frac{\gamma}{1 + \alpha^2}(\mathbf{m} \times (\mathbf{h}_{\text{eff}} + \mathbf{h}_{\text{ther}}) + \alpha \mathbf{m} \times (\mathbf{m} \times \mathbf{h}_{\text{eff}})) \\ & - \tau_{\text{STT}} \mathbf{m} \times (\mathbf{m} \times \mathbf{p}). \end{aligned} \quad (5)$$

Here, \mathbf{h}_{eff} is the effective field, \mathbf{h}_{ther} is the thermal field with magnitude given by Eq. (4), and τ_{STT} is the spin-transfer-torque magnitude given by [62,69]

$$\tau_{\text{STT}} = \frac{\gamma \hbar J}{2M_s e d (1 + \alpha^2)} \left(\frac{2P}{1 - P^2 \cos \varphi} \right), \quad (6)$$

where $\hbar/2$ is the magnitude of electron spin, J is the electric current density, P is the polarization, e is the electron charge, and d is the thickness of the free layer. Based on this set of equations, we can map the dynamics of the biological neuron to the dynamics of magnetization in the free layer of the proposed single MTJ device. The effective field, \mathbf{h}_{eff} , depends on the effective anisotropy vector, \mathbf{D} [80], and the dipolar field from the fixed layer, \mathbf{H}_F . We emphasize that, to obtain the spiking behavior, it is essential to consider a MTJ with an elliptical cross section, as in Ref. [62]. The elliptical shape breaks the in-plane rotational symmetry and favors a single in-plane direction and produces an in-plane unidirectional field, \mathbf{H}_F , from the polarizer. For details on macromagnetic simulations, see the Appendix. In the next section, we describe the results of the macrospin simulations.

III. RESULTS

Figure 2 shows the change in average resistance and average temperature for different applied currents. In Fig. 2(a), we characterize regions with two distinctive behaviors: (i) and (iii) where the magnetization is fixed by a strong bias given by the anisotropy or the STT, and (ii) where large-amplitude auto-oscillations are excited. Notice that the variation of temperature is essential for the firing behavior, which is characterized by a switch between steady and auto-oscillating states. The alternation is due to parameter scaling and the stochasticity, as seen in the bottom of Fig 2(a). Figure 2(b) shows the average temperature in terms of applied current, which is responsible for parameter scaling and the amplitude of the thermally induced stochasticity. Moreover, we emphasize that the stochasticity of the device due to thermal fluctuations also induces a small level of stochasticity of the firing behavior, which is relevant for neuromorphic applications.

Figure 3(a) shows the spiking frequency as a function of the applied current density emulating continuous firing under constant input. For low current densities, one observes higher frequencies, Fig. 3(b), while the frequency decreases for larger current densities, Fig. 3(c). The current-controlled frequency originates from the non-linear frequency shift linking the frequency and power of spintronic oscillators, as described in previous works and confirmed in several experiments [81–83]. The range of firing frequencies with the experimentally obtained parameters [62] is between 100 MHz and 3 GHz. Moreover, we notice that the period between spikes has small fluctuations associated with temperature-induced noise; see that in Fig. 3(c) the time difference between spikes is not constant. The thermal-induced stochasticity is important for biorealistic neural networks [1,22]. The other two thermal phenomena, i.e., parameter scaling and the resistance-variation-driven gain loss, are responsible for another important feature of the observed dynamics: the characteristic refractory period. The refractory period corresponds to a period succeeding the sharp spike where the output is lower than the average output. The lower output not only deters consecutive spikes but may also be used to tune the synapse weights. The latter allows for the implementation of STDP, which is a biologically plausible unsupervised learning mechanism [57–59]. Specifically, the two thermal phenomena generate a temporary stability of the strongly biased state, which has a lower resistance than the average resistance and prevents firings for a short period of time.

Besides emulating the H-H model, the versatile proposed device also works with current pulses within the LIF model. In the latter, pulses generate a time-dependent change in the system, which allows the pulses to be integrated or ignored, depending on their amplitude and relative time differences, see Figs. 4(a) and 4(b). To

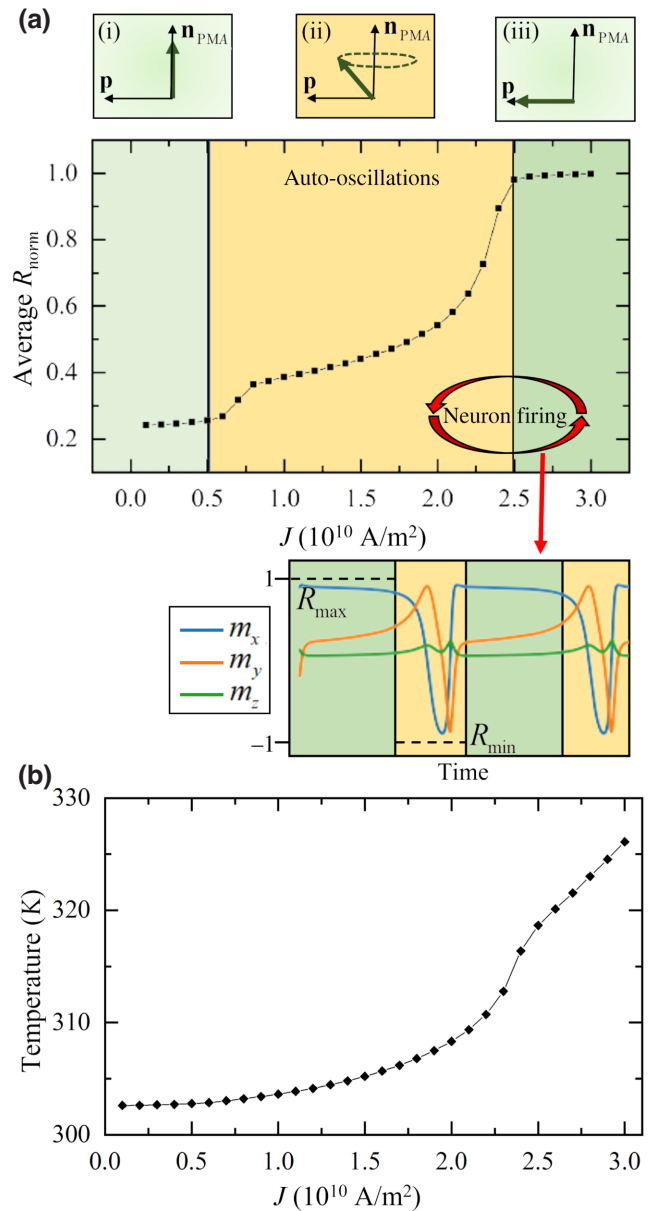


FIG. 2. Dependence of (a) the average normalized resistance and (b) temperature as a function of the applied current density. In (a), we identify three regions where (i) the magnetization is strongly biased towards the easy axis in the free layer (\mathbf{n}_{PMA}), (ii) there is an auto-oscillation around the easy axis of the free layer (\mathbf{n}_{PMA}), and (iii) the magnetization is strongly biased towards the direction of magnetization in the polarizer (\mathbf{p}). Firing behavior corresponds to a thermally induced alternation between auto-oscillation and the strongly biased state, as shown in the inset corresponding to the magnetization dynamics of the free layer, as shown in the right panel of (a). Notably, the resistance in this case is given by the m_x component, which is represented in blue.

demonstrate this functionality, we consider the initial or final current as a strong bias current that does not produce spikes and apply a sequence of pulses with a lower current, see Fig. 4(b). In the simulations, we consider both the

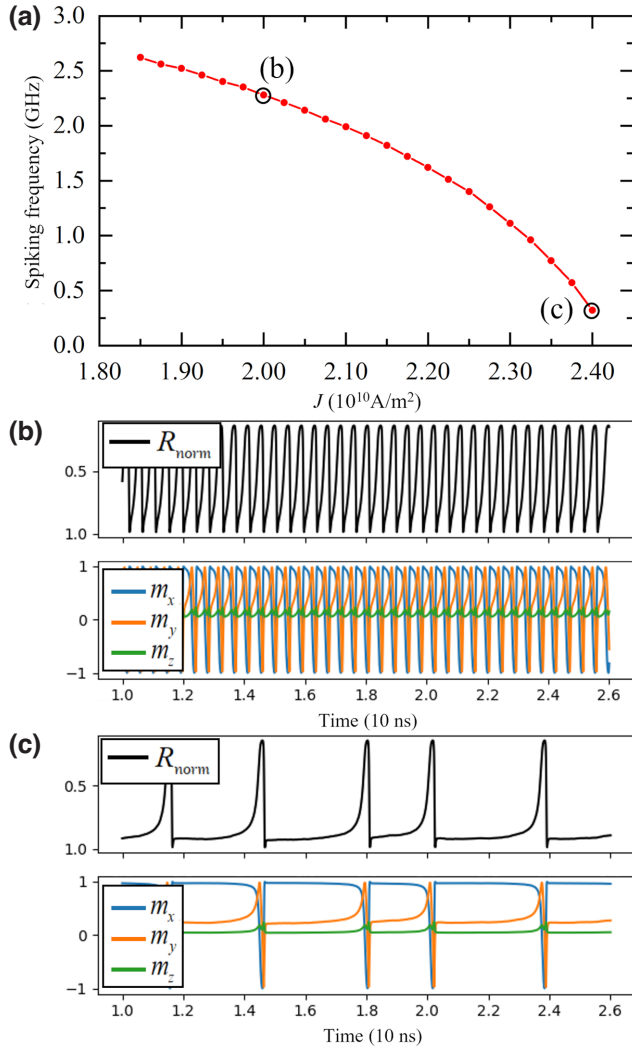


FIG. 3. (a) Frequency of neuron firing as a function of applied current density. (b),(c) Time-domain behavior of the resistance (top), magnetization components (middle; green, m_z ; orange, m_y ; blue, m_x), and temperature (bottom) for low (2×10^{10} A/m²) and high (2.4×10^{10} A/m²) current density, respectively.

size ($\Delta\tau$) and amplitude ($\Delta\iota$) of the pulses with respect to a higher bias current, $J_0 = 2.5 \times 10^{10}$ A/m², which shows no spikes. At higher amplitudes, $\Delta\iota$, the time to the first spike does not depend on the size of the pulses. To complement this analysis, we also show in Fig. 4(d) the time of the first spike for constant applied currents, corresponding to a pulse of infinite size. We notice that the time of the first pulse grows almost exponentially until a certain current where firings are no longer expected. Moreover, we notice that, for high $\Delta\iota$, i.e., low currents, the time to the first spike becomes rather constant at around 0.5 ns due to the existence of the refractory period.

This spiking behavior, which does not require a resetting mechanism, is rather robust as a function of different parameters, and the device properties can be tuned by

designing the thickness of the free layer and of the tunnelling layer, which influence the temperature variations.

IV. ANALOGY BETWEEN HODGKIN-HUXLEY AND LANDAU-LIFSHITZ-GILBERT MODELS

Previous attempts to emulate the H-H model with physical systems relied on coupling several memristors and were not area nor energy efficient [30,66,84,85]. We show, however, the possibility of emulating the H-H model by leveraging the intrinsically nonlinear dynamics of the proposed MTJ device combined with thermal effects. The H-H model is given by

$$C \frac{dV}{dt} = -F + I, \quad (7)$$

where V is the membrane potential, C is the neuron capacitance, F is the membrane internal current, and I is the sum of external and synaptic currents. The internal current, F , is a nonlinear function of the potential and three time- and voltage-dependent conductance variables (m , l , and n) associated with different biological mechanisms, such as potassium, sodium, and leakage currents [54,66,86]:

$$F = g_L(V - V_L) + g_K n^4(V - V_K) + g_{Na} h m^3(V - V_{Na}). \quad (8)$$

Here, g_L , g_K , and g_{Na} are constants, while V_L , V_K , and V_{Na} are voltage values associated with each mechanism. The channels m , l , and n evolve according to first-order time differential equations of the form

$$\frac{dx}{dt} = -\frac{1}{\tau_x}(x - x_0(V)), \quad (9)$$

where x stands for m , l , and n . Each channel is characterized by a different characteristic time, τ_x , the different timescales of which allow the model with four time-dependent channels to be reduced to only two [86,87]. We emphasize that the H-H model is obtained phenomenologically to fit experimental data. The model given by Eqs. (7)–(9) is highly nonlinear and cannot be easily simulated by software. For this reason, there have been several attempts to simplify the model to allow for easier computation [18,86,87]. We show that the magnetization dynamics is equally complex and can emulate the model from Eqs. (7)–(9) to produce the characteristic sharp spikes followed by the refractory period under constant input based on its own dynamics. We derive a minimal model based on the LLG Eq. (5) to constrain the rich magnetization dynamics to the specific device configuration and to allow for a clear understanding of the model comparability, see the Appendix for details. The minimal model is also useful for reducing the computational cost of numerical simulations. We consider the magnetization in spherical coordinates,

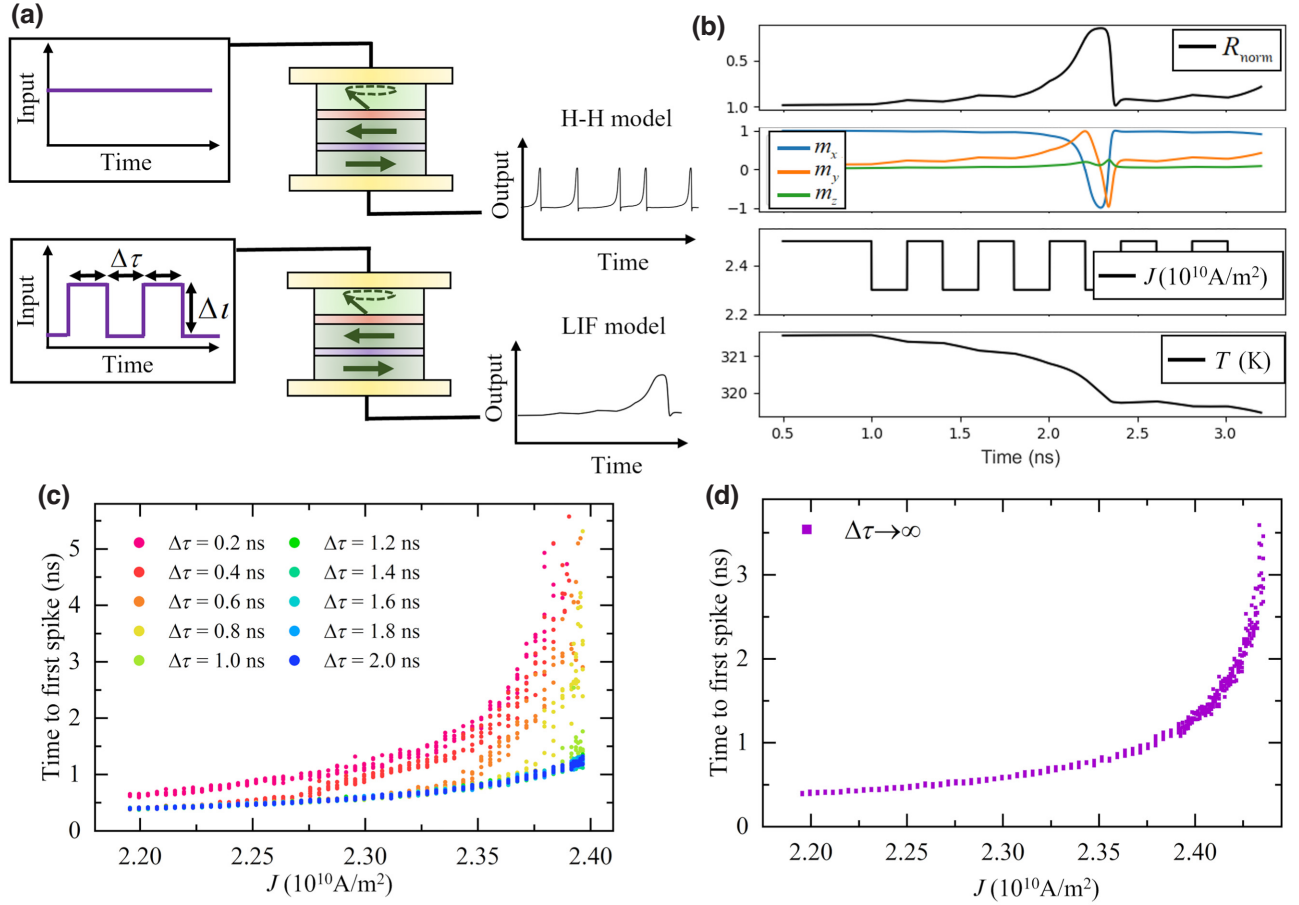


FIG. 4. (a) Difference between the H-H model and the LIF model. In the LIF model, we consider pulses of amplitude Δt and period $\Delta\tau$. (b) Evolution of the device properties in the presence of current pulses. From top to bottom panels, we show the normalized resistance, the evolution of the magnetization components, the profile of the applied current, and the temperature of the device. (c) Time between the first pulse and the first synapse. Different colors represent different pulse sizes, while the x axis represents the lowest-current value in the pulse. To include thermal-induced stochasticity, we simulate each pulse amplitude and size 5 times. (d) Time of the first synapse for a constant current.

$\mathbf{m} = \cos\theta(\hat{\mathbf{x}}\cos\varphi + \hat{\mathbf{y}}\sin\varphi) + \hat{\mathbf{z}}\sin\theta$, and by restricting it to the dynamics in the self-oscillation regime, with small variations of polar angle θ , we obtain the following equation of motion:

$$\frac{d\varphi}{dt} = -G + \iota, \quad (10a)$$

where

$$G = \frac{\iota_0}{1 - P(T)^2 \cos\varphi} \sin\varphi - \frac{\gamma\mu_0 M_s(T)}{2} (D_x + D_y - 2D_z + (D_x - D_y)\cos 2\varphi)\theta - \gamma H_F \cos\varphi\theta, \quad (10b)$$

with

$$\frac{d\theta}{dt} = -\frac{\iota_0}{1 - P(T)^2 \cos\varphi} \theta \cos\varphi - \frac{\gamma}{2} (2H_F \sin\varphi + (D_x - D_y)\mu_0 M_s(T) \sin 2\varphi). \quad (10c)$$

Here, $\iota_0 = \gamma\hbar PJ_0/M_s ed$ and $\iota = \gamma\hbar PJ/M_s ed$ are, respectively, the reference spin current, which biases the magnetization towards \mathbf{p} , and the spin-current difference, which allows for the firing behavior, as described in the previous section. We neglect damping because in the active region the magnetic losses are compensated for by the negative damping originating from the spin-transfer-torque. Moreover, notice that the model above emulates the H-H behavior, even in the absence of the dipolar field, i.e., $H_F = 0$. However, the field is necessary to set the tilted configuration of magnetization to achieve a low critical current for excitation of the self-oscillation of magnetization. The parameters $M_s(T)$ and $P(T)$ depend on temperature, as shown in Eqs. 3(a) and 3(b), and evolve according to the time evolution of the temperature given by Eq. (2). The model from Eqs. 10(a)–10(c), based on the LLG Eq. (5) reproduces the firing behavior reported in Figs. 1(b) and 2(a) emulating the H-H model.

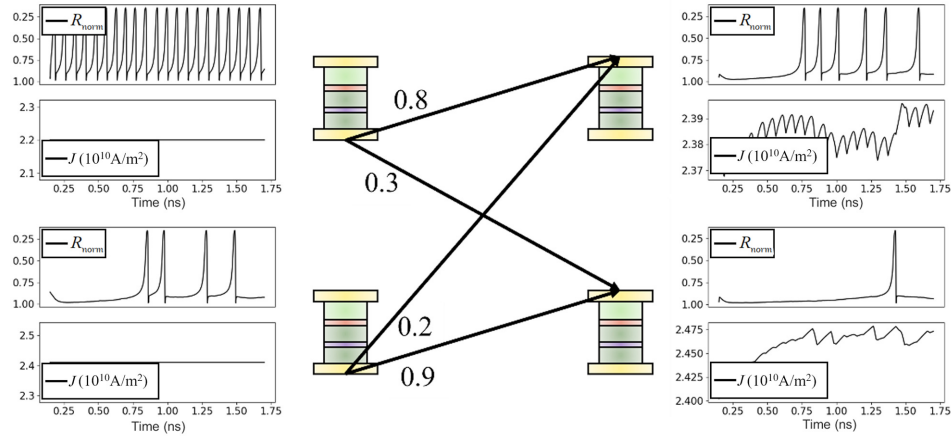
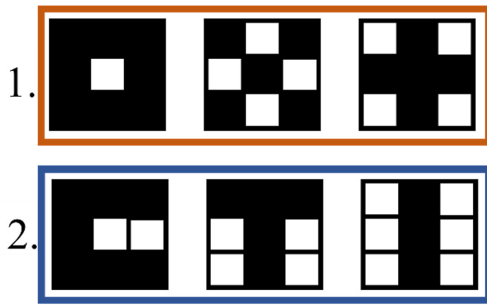
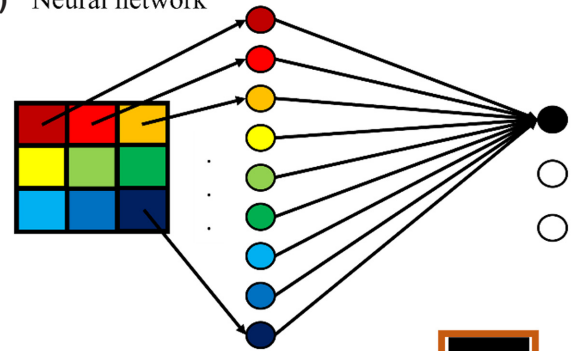
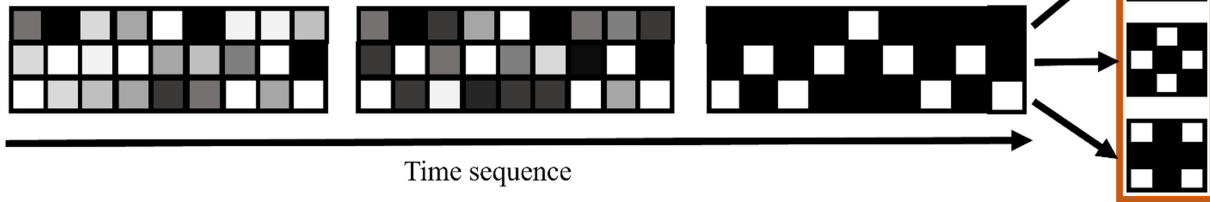
(a) Behavior of a simple SNN with 4 firing neurons**(b)** Input sets**(c)** Neural network**(d)** Evolution of weight matrix

FIG. 5. Example of a SNN built with the proposed MTJ device. (a) Behavior of a SNN with four neurons. Currents of the two input neurons are set as constants. For each MTJ, we show the behavior of the resistance (upper panel) and input current (lower panel). Input currents of the output neurons are generated according to Eq. (11), with the respective weights, W_{mn} , shown. (b) Two sets considered for verifying the learning process. (c) Sketch of the feed-forward all-connected SNN. Each pixel is associated with a single input neuron. (d) Evolution of the weight matrix. Starting from a random distribution of weights, after the training process, each figure can be represented by a single output neuron, which has the highest frequency.

The H-H model is characterized by four dynamic parameters (V , m , l , and n), while the LLG equation, including thermal effects, is described by three dynamic equations for θ , φ , and T , and two equations for the temperature-dependent material parameters, $P(T)$ and $M_s(T)$. Thus, the complexity of the MTJ model for the device is comparable to that of the H-H model, allowing the H-H model to be mapped onto the temperature-dependent LLG. In other words, it allows the biological evolution of the membrane potential in the H-H model to be mapped onto the tunable material properties and temperature dependence of

the device. In the proposed single-MTJ hardware implementation, the firing response is fully embedded in the dynamics of the MTJ, and no extra computation is required to simulate the H-H model. In particular, the channels with different timescales in Eq. (9) are mapped to the magnetization dynamics of θ , φ , and the temperature evolution of the material parameters, as discussed in Eqs. (2)–(4). Hence, the phenomenological constants of the H-H model are replaced by the geometric and magnetic properties of the MTJ, which can be engineered for the hardware requirements of analog SNN implementations. For a comparison

between the H-H model and the MTJ device proposed, see Table I.

V. UNSUPERVISED SPIKING NEURAL NETWORK

SNNs are optimal for processing time-dependent data, and the information is encoded in the rate or time difference of spikes [18,48,88–92]. To test the device concept in a simple SNN, we consider a rate-based information encoding. We employ the SNN to perform the classification of binarized images, where pixels can assume values “0” and “1” [93–95]. The SNN is given by two layers, an input and output layer, where the MTJs correspond to the firing neurons. For the current input of the first layer, we consider that 0 corresponds to a high current, where spikes are not observed, and 1 corresponds to a lower current, with a high frequency of spikes. The input current of output neurons, I_{out} , is given as a weighted voltage of the input neurons, V_{in} :

$$I_m(t) = \sum_{n=\text{input}} \chi_m(t) g(W_{mn} V_n(t)), \text{ where}$$

$$\frac{dg(V)}{dt} = \rho_g (V - V_{\text{ref}}) + \frac{g(V) - g(V_{\text{ref}})}{\tau_g}. \quad (11)$$

The function $g(V)$ is an exponential function that allows the integration of spikes over time and maintains a rather constant input current for the output neurons, and V_{ref} is a reference voltage [96]. The parameters ρ_g and τ_g are chosen according to the range of currents and frequency of spikes desired. The parameter $\chi_m(t) = \{0.1, 1\}$ emulates the lateral inhibition, i.e., if an output neuron spikes, the parameter $\chi_m(t)$ is decreased for all other neurons for a period of time given by the characteristic time interval between two spikes of the input neurons. The behavior for an example network with two input neurons and two output neurons can be seen in Fig. 5(a). We consider here the full macrospin model given in Eqs. (1)–(6) and detailed in the Appendix.

For the learning process, we consider an unsupervised mechanism, where the weights are updated according to the Hebbian and anti-Hebbian rule [94,95,97–99]. In particular, if an output neuron fires, the weight associated with the input neurons that have just spiked increases, while the weight associated with the input neurons that have not spiked recently decreases. Furthermore, we let the SNN weights evolve until an output neuron has a considerably higher frequency compared to the other neurons. To strengthen the learning, after this process, we fix the input currents of the output neurons according to the following algorithm: if the frequency of the output neuron is similar to or higher than the frequency obtained with other input images for that same output neuron, the input current is set to the lowest value of current achieved; otherwise, if the frequency is significantly lower than the frequency

obtained with other input images for that same output neuron, the neuron with the second-highest frequency is set with the lowest current achieved; the input of all other output neurons is fixed not to fire (i.e., the current associated with 0). With these fixed input currents on input and output neurons, the weights then evolve normally according to the Hebbian and anti-Hebbian learning.

We test the proposed SNN by considering two different sets of three patterns with 3×3 pixels, see Fig. 5(b). The SNN is made of nine input neurons, one for each pixel, and three output neurons, see Fig. 5(c). The pixels assume values 0 or 1, which uniquely identify two different currents with different firing rates (0, low frequency; 1, high frequency). The tests are performed by initiating the SNN with random weight matrices. After repeating a temporal sequence of each pattern from 3 to 5 times, the final weight matrix uniquely identifies each of the input patterns; see Fig. 5(d) for an example.

VI. SUMMARY AND CONCLUSIONS

Here, we design a single MTJ device to emulate bio-realistic spiking neurons with physical and geometrical parameters based on experimental data already published. The device emulates both the simpler LIF model and the more realistic H-H model without the need for a resetting mechanism. The proposed device works at room temperature and leverages two areas of physics to produce constant firing at constant input. We demonstrate the frequency dependence on the applied current, as well as a firing mechanism based on the amplitude and length of the input pulses. The rate of spikes is in the range from megahertz to gigahertz. The device presents several properties expected for the hardware implementation of biorealistic neurons, which include (i) being highly scalable, reproducible, and robust; (ii) the characteristic refractory period, showing a depression of the potential after the spike; and (iii) a small but nonvanishing stochasticity, which allows for random fluctuations without significantly increasing the error rate.

We verify the behavior of the device by simulating a spiking neural network to recognize different figures. The information is encoded in the spiking ratio. The neural network is successfully able to classify the figures. The largest set we consider is 3×3 pixels, due to computational limitations. It is important to emphasize that, while these calculations are usually computationally expensive, requiring a significant amount of memory and calculation time, the device’s inherent nonlinear and nonlocal time dynamics can realize the calculation rapidly at low power input.

Overall, the proposed device corresponds to a low-input highly reproducible scalable robust CMOS-compatible single MTJ working at room temperature that emulates the biorealistic H-H model. The device properties can be

TABLE II. Parameters used in the macrospin simulations at room temperature ($T = 300$ K).

Magnetic parameters	Symbol	Value	Geometric and thermal parameters	Symbol	Value
Saturation magnetization	$M_s (T = 300 \text{ K})$	$8.47 \times 10^5 \text{ A/m}$	Area of free layer	A	$6.25 \times 10^4 \text{ nm}^2$
Dipolar field from in-plane polarizer and pinning layer	H_F	7.7 mT	Thickness of free layer	d	1.6 nm
Polarization constant	$P (T = 300 \text{ K})$	0.78	Curie temperature	T_C	800 K
Gilbert damping	A	0.01	Ambient temperature	T_{amb}	300 K
Effective anisotropy vector	\mathbf{D}	(0.1, 0.2, -0.95)	Temperature decay time	τ_0	4 ns
Fixed-layer magnetization direction	\mathbf{n}_F	(1, 0, 0)	Heat efficiency	ρ/k_B	$3.0 \times 10^{14} \text{ K/Js}$
			Polarization scaling coefficient	ε_P	1.5

engineered to fit the network requirements by modifying the temperature gain (loss) of a previously experimentally realized MTJ concept. This proposal allows for an easy drop-in replacement in current SNN CMOS-based hardware implementations to increase area, energy, and memory efficiency.

ACKNOWLEDGMENTS

The research is supported by Project No. PRIN 2020LWPKH7 funded by the Italian Ministry of University and Research. D.R.R., R.M., M.C., and G.F. are members of the Petaspin team and acknowledge support from

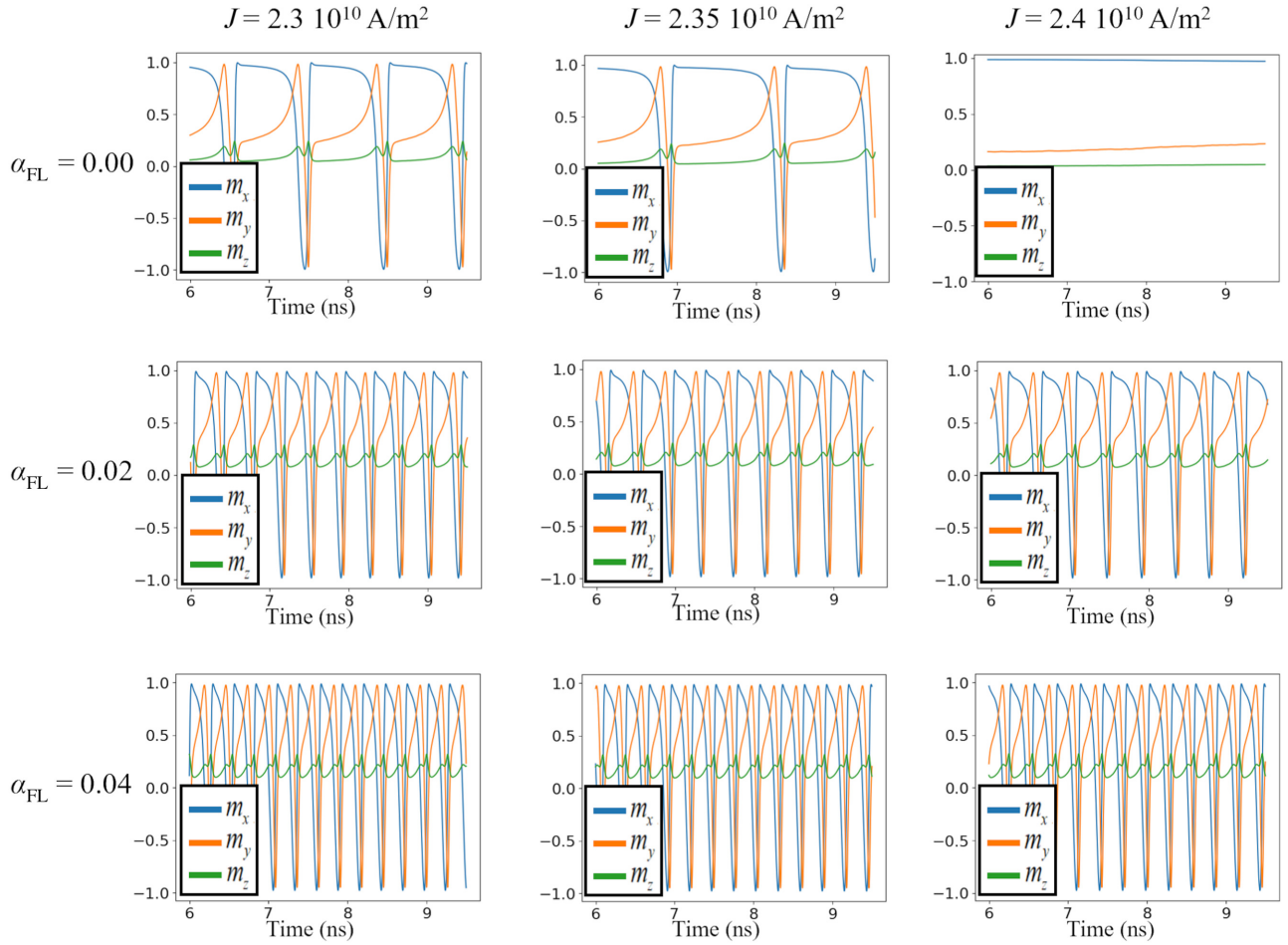


FIG. 6. Behavior of magnetization dynamics for different currents and including the fieldlike torque. Material parameters are those give in Table II.

the Petaspin Association (<https://www.petaspin.com/>). D.R.R. also acknowledges funding from the Ministero dell'Università e della Ricerca, Decreto Ministeriale n.1062 del 10/08/2021 (PON Ricerca e Innovazione). Z. M. Zeng would like to acknowledge the National Natural Science Foundation of China (No. 11974379) and K. C. Wong Education Foundation (No. GJTD-2019-14).

APPENDIX: MICROMAGNETIC MODEL

In this work, we consider a MTJ experimentally realized in Ref. [62] with a MgO barrier sandwiched between a free layer with perpendicular magnetic anisotropy (PMA) and an in-plane-magnetized fixed layer, see Fig. 1(a) in the main text. The magnetization of the free layer is described by a single magnetization vector, which evolves over time according to the LLG Eq. (5) of the main text. The effective magnetic field, \mathbf{h}_{eff} , is given by

$$\mathbf{h}_{\text{eff}} = -\mu_0 M_s (D_x m_x \hat{\mathbf{x}} + D_y m_y \hat{\mathbf{y}} + D_z m_z \hat{\mathbf{z}}) - H_F \mathbf{n}_F, \quad (\text{A1})$$

where $\mathbf{m} = \mathbf{M}/M_s$ is the unitary magnetization vector of the free layer; M_s is the magnetization saturation; \mathbf{D} is the effective anisotropy vector [80], which includes the material anisotropy and magnetostatic fields; and μ_0 is the vacuum permeability. We also consider an external field due to coupling to the fixed layers with strength and direction given by H_F , proportional to the magnetization of the fixed layer, and \mathbf{n}_F , respectively. The thermal field is modeled by Gaussian noise with a magnitude given by

$$\mathbf{h}_{\text{ther}} = h_{\text{ther}} \mathbf{n}_t, \quad (\text{A2a})$$

with

$$\langle n_{t,i}(t) n_{t,j}(t') \rangle = \delta_{ij} \delta(t - t') \quad (\text{A2b})$$

being the time correlation for the randomized unitary vector, \mathbf{n}_t , and the magnitude of h_{ther} is given by Eq. (4). The parameters used in the simulations are given in Table II.

To derive the minimal model from 10(a)–10(c), we consider the LLG Eq. (5) and substitute the unitary magnetization in the spherical coordinates, $\mathbf{m} = \cos \theta (\hat{\mathbf{x}} \cos \varphi + \hat{\mathbf{y}} \sin \varphi) + \hat{\mathbf{z}} \sin \theta$. Notably, for \mathbf{m} parallel to the easy axis, $\theta = \pi/2$, while, for \mathbf{m} along \mathbf{p} , $\theta = \varphi = 0$. We expand the LLG equation to linear order in θ , to consider auto-oscillations at high input currents. Thermal effects are included in the minimal model, Eqs. 10(a)–(c), as effective changes to the material parameter values in the LLG Eq. (5), shown in Eqs. (2)–(4).

Moreover, in the main text, we neglect the contribution of fieldlike torques. We can include such torques by adding the following term to the LLG Eq. (5):

$$\boldsymbol{\tau}_{\text{FL}} = \alpha_{\text{FL}} \tau_{\text{STT}} \mathbf{m} \times \mathbf{p}, \quad (\text{A3})$$

where α_{FL} is a coefficient for the strength of the fieldlike torque and is often assumed to be small (i.e., $\alpha_{\text{FL}} \ll 1$) [100]. Figure 6 shows the spiking behavior for different currents and α_{FL} . We notice that the fieldlike torque qualitatively increases the frequency of the spikes, requiring a higher current for a lower spiking frequency.

- [1] D. Marković, A. Mizrahi, D. Querlioz, and J. Grollier, Physics for neuromorphic computing, *Nat. Rev. Phys.* **2**, 499 (2020).
- [2] G. W. Burr, R. M. Shelby, A. Sebastian, S. Kim, S. Kim, S. Sidler, K. Virwani, M. Ishii, P. Narayanan, A. Fumarola, L. L. Sanches, I. Boybat, M. Le Gallo, K. Moon, J. Woo, H. Hwang, and Y. Leblebici, Neuromorphic computing using non-volatile memory, *Adv. Phys.* **X 2**, 89 (2017).
- [3] K. Roy, A. Jaiswal, and P. Panda, Towards spike-based machine intelligence with neuromorphic computing, *Nature* **575**, 607 (2019).
- [4] C. D. Schuman, S. R. Kulkarni, M. Parsa, J. P. Mitchell, P. Date, and B. Kay, Opportunities for neuromorphic computing algorithms and applications, *Nat. Comput. Sci.* **2**, 10 (2022).
- [5] S. Ghosh-Dastidar and H. Adeli, Spiking neural networks, *Int. J. Neural Syst.* **19**, 295 (2009).
- [6] W. Maass, Networks of spiking neurons: The third generation of neural network models, *Neural Networks* **10**, 1659 (1997).
- [7] D. V. Christensen, *et al.*, Roadmap on neuromorphic computing and engineering, *Neuromorphic Comput. Eng.* **2**, 022501 (2022).
- [8] M. Bouvier, A. Valentian, T. Mesquida, F. Rumens, M. Reyboz, E. Vianello, and E. Beigne, Spiking neural networks hardware implementations and challenges, *ACM J. Emerg. Technol. Comput. Syst.* **15**, 1 (2019).
- [9] A. Sengupta, Y. Ye, R. Wang, C. Liu, and K. Roy, Going deeper in spiking neural networks: VGG and residual architectures, *Front. Neurosci.* **13**, 95 (2019).
- [10] A. Gupta and L. N. Long, in *IEEE International Conference on Neural Networks - Conference Proceedings* (IEEE, 2007), pp. 53–58.
- [11] J. J. Wade, L. J. McDaid, J. A. Santos, and H. M. Sayers, SWAT: A spiking neural network training algorithm for classification problems, *IEEE Trans. Neural Networks* **21**, 1817 (2010).
- [12] S. Ghosh-Dastidar and H. Adeli, Improved spiking neural networks for EEG classification and epilepsy and seizure detection, *Integr. Comput. Aided. Eng.* **14**, 187 (2007).
- [13] X. Jin, S. B. Furber, and J. V. Woods, in *Proceedings of the International Joint Conference on Neural Networks* (2008), pp. 2812.
- [14] X. Jin, M. Luján, L. A. Plana, S. Davies, S. Temple, and S. B. Furber, Modeling spiking neural networks on SpiNNaker, *Comput. Sci. Eng.* **12**, 91 (2010).
- [15] S. B. Furber, F. Galluppi, S. Temple, and L. A. Plana, The SpiNNaker project, *Proc. IEEE* **102**, 652 (2014).

- [16] J. Schemmel, in *Encyclopedia of Computational Neuroscience*, edited by D. Jaeger and R. Jung (Springer, New York, NY, 2014), pp. 1–4.
- [17] D. Goodman, Brian: A simulator for spiking neural networks in PYTHON, *Front. Neuroinform.* **2**, 5 (2008).
- [18] C. Teeter, R. Iyer, V. Menon, N. Gouwens, D. Feng, J. Berg, A. Szafer, N. Cain, H. Zeng, M. Hawrylycz, C. Koch, and S. Mihalas, Generalized leaky integrate-and-fire models classify multiple neuron types, *Nat. Commun.* **9**, 709 (2018).
- [19] G. Finocchio, *et al.*, Roadmap for Unconventional Computing with Nanotechnology, arXiv:2301.06727 (2023).
- [20] W. Haensch, T. Gokmen, and R. Puri, The next generation of deep learning hardware: Analog computing, *Proc. IEEE* **107**, 108 (2019).
- [21] H. T. Siegelmann, *Neural Networks and Analog Computation* (Birkhäuser Boston, Boston, MA, 1999).
- [22] B. Dieny, *et al.*, Opportunities and challenges for spintronics in the microelectronics industry, *Nat. Electron.* **3**, 446 (2020).
- [23] P. A. Merolla, *et al.*, A million spiking-neuron integrated circuit with a scalable communication network and interface, *Science* **345**, 668 (2014).
- [24] M. Davies, *et al.*, Loihi: A neuromorphic manycore processor with on-chip learning, *IEEE Micro.* **38**, 82 (2018).
- [25] G. Indiveri, in *Proceedings of the 2003 International Symposium on Circuits and Systems, ISCAS '03* (IEEE, 2003), Vol. 4, pp. IV-820–IV-823.
- [26] Q. Wan, M. T. Sharbati, J. R. Erickson, Y. Du, and F. Xiong, Emerging artificial synaptic devices for neuromorphic computing, *Adv. Mater. Technol.* **4**, 1900037 (2019).
- [27] K. S. Kravtsov, M. P. Fok, P. R. Prucnal, and D. Rosenbluth, Ultrafast all-optical implementation of a leaky integrate-and-fire neuron, *Opt. Express* **19**, 2133 (2011).
- [28] S. Dutta, V. Kumar, A. Shukla, N. R. Mohapatra, and U. Ganguly, Leaky integrate and fire neuron by charge-discharge dynamics in floating-body MOSFET, *Sci. Rep.* **7**, 8257 (2017).
- [29] D. Rajasekharan, A. Gaidhane, A. R. Trivedi, and Y. S. Chauhan, Ferroelectric FET-based implementation of FitzHugh-Nagumo neuron model, *IEEE Trans. Comput. Des. Integr. Circuits Syst.* **41**, 2107 (2022).
- [30] L. Chua, Memristor, Hodgkin–Huxley, and edge of chaos, *Nanotechnology* **24**, 383001 (2013).
- [31] D. Querlioz, W. S. Zhao, P. Dollfus, J.-O. Klein, O. Bichler, and C. Gamrat, in *Proceedings of the 2012 IEEE/ACM International Symposium on Nanoscale Architectures* (ACM, New York, NY, USA, 2012), pp. 203–210.
- [32] A. Afifi, A. Ayatollahi, and F. Raissi, in *2009 European Conference on Circuit Theory and Design* (IEEE, 2009), pp. 563–566.
- [33] A. Natarajan and J. Hasler, Hodgkin-Huxley Neuron and FPAA dynamics, *IEEE Trans. Biomed. Circuits Syst.* **12**, 918 (2018).
- [34] J.-Q. Yang, R. Wang, Z.-P. Wang, Q.-Y. Ma, J.-Y. Mao, Y. Ren, X. Yang, Y. Zhou, and S.-T. Han, Leaky integrate-and-fire neurons based on perovskite memristor for spiking neural networks, *Nano Energy* **74**, 104828 (2020).
- [35] R. Khymyn, I. Lisenkov, J. Voorheis, O. Sulymenko, O. Prokopenko, V. Tiberkevich, J. Akerman, and A. Slavin, Ultra-fast artificial neuron: Generation of picosecond-duration spikes in a current-driven antiferromagnetic auto-oscillator, *Sci. Rep.* **8**, 15727 (2018).
- [36] A. Kurenkov, S. DuttaGupta, C. Zhang, S. Fukami, Y. Horio, and H. Ohno, Artificial neuron and synapse realized in an antiferromagnet/ferromagnet heterostructure using dynamics of spin-orbit torque switching, *Adv. Mater.* **31**, 1900636 (2019).
- [37] A. F. Vincent, J. Larroque, N. Locatelli, N. Ben Romdhane, O. Bichler, C. Gamrat, W. S. Zhao, J.-O. Klein, S. Galdin-Retailleau, and D. Querlioz, Spin-transfer torque magnetic memory as a stochastic memristive synapse for neuromorphic systems, *IEEE Trans. Biomed. Circuits Syst.* **9**, 166 (2015).
- [38] A. Sengupta and K. Roy, Short-Term Plasticity and Long-Term Potentiation in Magnetic Tunnel Junctions: Towards Volatile Synapses, *Phys. Rev. Appl.* **5**, 024012 (2016).
- [39] J. Grollier, D. Querlioz, and M. D. Stiles, Spintronic nanodevices for bioinspired computing, *Proc. IEEE* **104**, 2024 (2016).
- [40] G. Finocchio, M. Di Ventra, K. Y. Camsari, K. Everschor-Sitte, P. Khalili Amiri, and Z. Zeng, The promise of spintronics for unconventional computing, *J. Magn. Magn. Mater.* **521**, 167506 (2021).
- [41] R. De Rose, M. Lanuzza, F. Crupi, G. Siracusano, R. Tomasello, G. Finocchio, M. Carpentieri, and M. Alioto, A variation-aware timing modeling approach for write operation in hybrid CMOS/STT-MTJ circuits, *IEEE Trans. Circuits Syst. I Regul. Pap.* **65**, 1086 (2018).
- [42] J. Puebla, J. Kim, K. Kondou, and Y. Otani, Spintronic devices for energy-efficient data storage and energy harvesting, *Commun. Mater.* **1**, 24 (2020).
- [43] S. Umesh and S. Mittal, A survey of spintronic architectures for processing-in-memory and neural networks, *J. Syst. Archit.* **97**, 349 (2019).
- [44] A. Sengupta, P. Panda, P. Wijesinghe, Y. Kim, and K. Roy, Magnetic tunnel junction mimics stochastic cortical spiking neurons, *Sci. Rep.* **6**, 30039 (2016).
- [45] G. Srinivasan, A. Sengupta, and K. Roy, Magnetic tunnel junction based long-term short-term stochastic synapse for a spiking neural network with on-chip STDP learning, *Sci. Rep.* **6**, 29545 (2016).
- [46] A. Jaiswal, S. Roy, G. Srinivasan, and K. Roy, Proposal for a leaky-integrate-fire spiking neuron based on magnetoelectric switching of ferromagnets, *IEEE Trans. Electron. Devices* **64**, 1818 (2017).
- [47] W. Lv, J. Cai, H. Tu, L. Zhang, R. Li, Z. Yuan, G. Finocchio, S. Li, X. Sun, L. Bian, B. Zhang, R. Xiong, and Z. Zeng, Stochastic artificial synapses based on nanoscale magnetic tunnel junction for neuromorphic applications, *Appl. Phys. Lett.* **121**, 232406 (2022).
- [48] M. Romera, P. Talatchian, S. Tsunegi, K. Yakushiji, A. Fukushima, H. Kubota, S. Yuasa, V. Cros, P. Bortolotti, M. Ernout, D. Querlioz, and J. Grollier, Binding events through the mutual synchronization of spintronic nano-neurons, *Nat. Commun.* **13**, 883 (2022).

- [49] J. Torrejon, M. Riou, F. A. Araujo, S. Tsunegi, G. Khalsa, D. Querlioz, P. Bortolotti, V. Cros, K. Yakushiji, A. Fukushima, H. Kubota, S. Yuasa, M. D. Stiles, and J. Grollier, Neuromorphic computing with nanoscale spintronic oscillators, *Nature* **547**, 428 (2017).
- [50] C. M. Liyanagedera, A. Sengupta, A. Jaiswal, and K. Roy, Stochastic Spiking Neural Networks Enabled by Magnetic Tunnel Junctions: From Nontelegraphic to Telegraphic Switching Regimes, *Phys. Rev. Appl.* **8**, 064017 (2017).
- [51] B. R. Zink, Y. Lv, and J. P. Wang, Telegraphic switching signals by magnet tunnel junctions for neural spiking signals with high information capacity, *J. Appl. Phys.* **124**, 152121 (2018).
- [52] Q. Yang, R. Mishra, Y. Cen, G. Shi, R. Sharma, X. Fong, and H. Yang, Spintronic integrate-fire-reset neuron with stochasticity for neuromorphic computing, *Nano Lett.* **22**, 8437 (2022).
- [53] J. Feng, Is the integrate-and-fire model good enough?—A review, *Neural Networks* **14**, 955 (2001).
- [54] L. F. Abbott and T. B. Kepler, *Model Neurons: From Hodgkin-Huxley to Hopfield*, in *Statistical Mechanics of Neural Networks* (Springer Berlin Heidelberg, Berlin, Heidelberg, 1990), pp. 5–18.
- [55] A. L. Hodgkin and A. F. Huxley, A quantitative description of membrane current and its application to conduction and excitation in nerve, *J. Physiol* **117**, 500 (1952).
- [56] A. Taherkhani, A. Belatreche, Y. Li, G. Cosma, L. P. Maguire, and T. M. McGinnity, A review of learning in biologically plausible spiking neural networks, *Neural Networks* **122**, 253 (2020).
- [57] E. M. Izhikevich, Solving the distal reward problem through linkage of STDP and dopamine signaling, *Cereb. Cortex*. **17**, 2443 (2007).
- [58] T. Serrano-Gotarredona, T. Masquelier, T. Prodromakis, G. Indiveri, and B. Linares-Barranco, STDP and STDP variations with memristors for spiking neuromorphic learning systems, *Front. Neurosci.* **7**, 2 (2013).
- [59] S. R. Kheradpisheh, M. Ganjtabesh, S. J. Thorpe, and T. Masquelier, STDP-based spiking deep convolutional neural networks for object recognition, *Neural Networks* **99**, 56 (2018).
- [60] J. L. Lobo, J. Del Ser, A. Bifet, and N. Kasabov, Spiking neural networks and online learning: An overview and perspectives, *Neural Networks* **121**, 88 (2020).
- [61] G. Finocchio, I. N. Krivorotov, X. Cheng, L. Torres, and B. Azzarboni, Micromagnetic understanding of stochastic resonance driven by spin-transfer-torque, *Phys. Rev. B* **83**, 134402 (2011).
- [62] Z. Zeng, G. Finocchio, B. Zhang, P. K. Amiri, J. A. Katine, I. N. Krivorotov, Y. Huai, J. Langer, B. Azzarboni, K. L. Wang, and H. Jiang, Ultralow-current-density and bias-field-free spin-transfer nano-oscillator, *Sci. Rep.* **3**, 1426 (2013).
- [63] A. Roxin, N. Brunel, D. Hansel, G. Mongillo, and C. van Vreeswijk, On the distribution of firing rates in networks of cortical neurons, *J. Neurosci.* **31**, 16217 (2011).
- [64] M. Nawrot, A. Aertsen, and S. Rotter, Single-trial estimation of neuronal firing rates: From single-neuron spike trains to population activity, *J. Neurosci. Methods* **94**, 81 (1999).
- [65] R. N. Miller and J. Rinzel, The dependence of impulse propagation speed on firing frequency, dispersion, for the Hodgkin-Huxley model, *Biophys. J.* **34**, 227 (1981).
- [66] L. Chua, V. Sbitnev, and H. Kim, Hodgkin-Huxley axon is made of memristors, *Int. J. Bifurc. Chaos* **22**, 1230011 (2012).
- [67] K. Campbell, L. Staugler, and A. Arnold, Estimating time-varying applied current in the Hodgkin-Huxley model, *Appl. Sci.* **10**, 550 (2020).
- [68] J. C. Slonczewski, Current-driven excitation of magnetic multilayers, *J. Magn. Magn. Mater.* **159**, L1 (1996).
- [69] Z. M. Zeng, P. Khalili Amiri, J. A. Katine, J. Langer, K. L. Wang, and H. W. Jiang, Nanoscale magnetic tunnel junction sensors with perpendicular anisotropy sensing layer, *Appl. Phys. Lett.* **101**, 062412 (2012).
- [70] B. Fang, M. Carpentieri, X. Hao, H. Jiang, J. A. Katine, I. N. Krivorotov, B. Ocker, J. Langer, K. L. Wang, B. Zhang, B. Azzarboni, P. K. Amiri, G. Finocchio, and Z. Zeng, Giant spin-torque diode sensitivity in the absence of bias magnetic field, *Nat. Commun.* **7**, 11259 (2016).
- [71] Z. Zeng, G. Finocchio, and H. Jiang, Spin transfer nano-oscillators, *Nanoscale* **5**, 2219 (2013).
- [72] R. Tomasello, K. Y. Guslienko, M. Ricci, A. Giordano, J. Barker, M. Carpentieri, O. Chubykalo-Fesenko, and G. Finocchio, Origin of temperature and field dependence of magnetic skyrmion size in ultrathin nanodots, *Phys. Rev. B* **97**, 060402(R) (2018).
- [73] J. G. Alzate, P. Khalili Amiri, G. Yu, P. Upadhyaya, J. A. Katine, J. Langer, B. Ocker, I. N. Krivorotov, and K. L. Wang, Temperature dependence of the voltage-controlled perpendicular anisotropy in nanoscale MgO|CoFeB|Ta magnetic tunnel junctions, *Appl. Phys. Lett.* **104**, 112410 (2014).
- [74] C. H. Shang, J. Nowak, R. Jansen, and J. S. Moodera, Temperature dependence of magnetoresistance and surface magnetization in ferromagnetic tunnel junctions, *Phys. Rev. B* **58**, R2917 (1998).
- [75] A. H. Davis, J. M. MacLaren, and P. LeClair, Inherent temperature effects in magnetic tunnel junctions, *J. Appl. Phys.* **89**, 7567 (2001).
- [76] W. F. Brown, Thermal fluctuations of a single-domain particle, *Phys. Rev.* **130**, 1677 (1963).
- [77] G. Deco, E. T. Rolls, and R. Romo, Stochastic dynamics as a principle of brain function, *Prog. Neurobiol.* **88**, 1 (2009).
- [78] A. Giordano, G. Finocchio, L. Torres, M. Carpentieri, and B. Azzarboni, Semi-implicit integration scheme for Landau-Lifshitz-Gilbert-Slonczewski equation, *J. Appl. Phys.* **111**, 07D112 (2012).
- [79] J. Xiao, A. Zangwill, and M. D. Stiles, Macrospin models of spin transfer dynamics, *Phys. Rev. B* **72**, 014446 (2005).
- [80] G. Siracusano, R. Tomasello, M. D'Aquino, V. Puliafito, A. Giordano, B. Azzarboni, P. Branganca, G. Finocchio, and M. Carpentieri, Description of statistical switching in perpendicular STT-MRAM within an analytical and numerical micromagnetic framework, *IEEE Trans. Magn.* **54**, 1 (2018).

- [81] A. Slavin and V. Tiberkevich, Nonlinear auto-oscillator theory of microwave generation by spin-polarized current, *IEEE Trans. Magn.* **45**, 1875 (2009).
- [82] A. Hamadeh, G. de Loubens, V. V. Naletov, J. Grollier, C. Ulysse, V. Cros, and O. Klein, Autonomous and forced dynamics in a spin-transfer nano-oscillator: Quantitative magnetic-resonance force microscopy, *Phys. Rev. B* **85**, 140408 (2012).
- [83] M. Rajabali, R. Ovcharov, R. Khymyn, H. Fulara, A. Kumar, A. Litvinenko, M. Zahedinejad, A. Houshang, A. A. Awad, and J. Åkerman, Injection Locking of Linear-like and Soliton Spin-Wave Modes in Nanoconstriction Spin Hall Nano-Oscillators, *Phys. Rev. Appl.* **19**, 034070 (2023).
- [84] X. Hu and C. Liu, Dynamic property analysis and circuit implementation of simplified memristive Hodgkin–Huxley neuron model, *Nonlinear Dyn.* **97**, 1721 (2019).
- [85] M. P. Sah, Hyongsuk Kim, and L. O. Chua, Brains are made of memristors, *IEEE Circuits Syst. Mag.* **14**, 12 (2014).
- [86] L. F. Abbott and T. B. Kepler, in *Statistical Mechanics of Neural Networks*, edited by L. Garrido (Springer, Berlin, Heidelberg, 2008), pp. 5–18.
- [87] E. M. Izhikevich, Which model to use for cortical spiking neurons?, *IEEE Trans. Neural Networks* **15**, 1063 (2004).
- [88] J. H. Lee, T. Delbruck, and M. Pfeiffer, Training deep spiking neural networks using backpropagation, *Front. Neurosci.* **10**, 508 (2016).
- [89] A. Tavanaei, M. Ghodrati, S. R. Kheradpisheh, T. Masquelier, and A. Maida, Deep learning in spiking neural networks, *Neural Networks* **111**, 47 (2019).
- [90] J. J. Hopfield and C. D. Brody, What is a moment? Transient synchrony as a collective mechanism for spatiotemporal integration, *Proc. Natl. Acad. Sci. U. S. A.* **98**, 1282 (2001).
- [91] M. Hejda, J. A. Alanis, I. Ortega-Piwonka, J. Lourenço, J. Figueiredo, J. Javaloyes, B. Romeira, and A. Hurtado, Resonant Tunneling Diode Nano-optoelectronic Excitable Nodes for Neuromorphic Spike-Based Information Processing, *Phys. Rev. Appl.* **17**, 024072 (2022).
- [92] M.-H. Wu, I.-T. Wang, M.-C. Hong, K.-M. Chen, Y.-C. Tseng, J.-H. Wei, and T.-H. Hou, Stochastic Switching in a Magnetic-Tunnel-Junction Neuron and a Bias-Dependent Néel-Arrhenius Model, *Phys. Rev. Appl.* **18**, 064034 (2022).
- [93] A. Amirsoleimani, M. Ahmadi, A. Ahmadi, and M. Boukadoum, in *2016 IEEE International Conference on Electronics, Circuits and Systems (ICECS)* (IEEE, 2016), pp. 81–84.
- [94] S. Fukami and H. Ohno, Perspective: Spintronic synapse for artificial neural network, *J. Appl. Phys.* **124**, 151904 (2018).
- [95] J. Feldmann, N. Youngblood, C. D. Wright, H. Bhaskaran, and W. H. P. Pernice, All-optical spiking neurosynaptic networks with self-learning capabilities, *Nature* **569**, 208 (2019).
- [96] A. Delorme and S. J. Thorpe, SpikeNET: An event-driven simulation package for modelling large networks of spiking neurons, *Networks Comput. Neural Syst.* **14**, 613 (2003).
- [97] D. O. Hebb, *The Organization of Behavior* (Psychology Press, New York, 2005).
- [98] A. Sengupta, A. Banerjee, and K. Roy, Hybrid Spintronic-CMOS Spiking Neural Network with On-Chip Learning: Devices, Circuits, and Systems, *Phys. Rev. Appl.* **6**, 064003 (2016).
- [99] D. H. Ackley, G. E. Hinton, and T. J. Sejnowski, A learning algorithm for Boltzmann machines, *Cognit. Sci.* **9**, 147 (1985).
- [100] S. Zhang, P. M. Levy, and A. Fert, Mechanisms of Spin-Polarized Current-Driven Magnetization Switching, *Phys. Rev. Lett.* **88**, 236601 (2002).